


















Large intrinsic anomalous Hall effect in SrIrO₃ induced by magnetic proximity effect

Myoung-Woo Yoo¹, J. Tornos², A. Sander ¹, Ling-Fang Lin ^{3,4}, Narayan Mohanta ⁵, A. Peralta ², D. Sanchez-Manzano ², F. Gallego², D. Haskel⁶, J. W. Freeland ⁶, D. J. Keavney ⁶, Y. Choi ⁶, J. Stremper ⁶, X. Wang⁷, M. Cabero ^{8,9}, Hari Babu Vasili¹⁰, Manuel Valvidares ¹⁰, G. Sanchez-Santolino ², J. M. Gonzalez-Calbet ^{9,11}, A. Rivera ², C. Leon², S. Rosenkranz ¹², M. Bibes ¹, A. Barthélemy¹, A. Anane ¹, Elbio Dagotto ^{3,5}, S. Okamoto ⁵, S. G. E. te Velthuis¹², J. Santamaria ²  & Javier E. Villegas ¹

The anomalous Hall effect (AHE) is an intriguing transport phenomenon occurring typically in ferromagnets as a consequence of broken time reversal symmetry and spin-orbit interaction. It can be caused by two microscopically distinct mechanisms, namely, by skew or side-jump scattering due to chiral features of the disorder scattering, or by an intrinsic contribution directly linked to the topological properties of the Bloch states. Here we show that the AHE can be artificially engineered in materials in which it is originally absent by combining the effects of symmetry breaking, spin orbit interaction and proximity-induced magnetism. In particular, we find a strikingly large AHE that emerges at the interface between a ferromagnetic manganite (La_{0.7}Sr_{0.3}MnO₃) and a semimetallic iridate (SrIrO₃). It is intrinsic and originates in the proximity-induced magnetism present in the narrow bands of strong spin-orbit coupling material SrIrO₃, which yields values of anomalous Hall conductivity and Hall angle as high as those observed in bulk transition-metal ferromagnets. These results demonstrate the interplay between correlated electron physics and topological phenomena at interfaces between 3d ferromagnets and strong spin-orbit coupling 5d oxides and trace an exciting path towards future topological spintronics at oxide interfaces.

¹Unité Mixte de Physique, CNRS, Thales, Université Paris-Saclay, Palaiseau, France. ²GFMC, Dept. Física de Materiales, Facultad de Física, Universidad Complutense, Madrid, Spain. ³Department of Physics and Astronomy, University of Tennessee, Knoxville, TN, USA. ⁴School of Physics, Southeast University, Nanjing, China. ⁵Materials Science and Technology Division, Oak Ridge National Laboratory, Oak Ridge, TN, USA. ⁶Advanced Photon Source Argonne National Laboratory, Lemont, IL, USA. ⁷Department of Physics, Bryn Mawr College, Bryn Mawr, PA, USA. ⁸IMDEA Nanoscience Campus Universidad Autónoma, Cantoblanco, Spain. ⁹Centro Nacional de Microscopia Electrónica, Universidad Complutense, Madrid, Spain. ¹⁰CELLS-ALBA Synchrotron Radiation Facility, Cerdanyola del Valles, Spain. ¹¹Department Química Inorgánica, Facultad de Química, Universidad Complutense, Madrid, Spain. ¹²Materials Science Division, Argonne National Laboratory, Lemont, IL, USA. ✉email: jacsan@ucm.es

The Hall resistivity of ferromagnets has been shown to follow the empirical relation¹ $\rho_{xy} = R_0 H_z + \Delta\rho_{xy}^{\text{AHE}} M_z$. The first term is the ordinary Hall resistivity, and the normal Hall parameter R_0 depends basically on the carrier density. The second term scales with the sample magnetization M_z and is the anomalous Hall effect (AHE), which is characterized by the anomalous Hall coefficient $\Delta\rho_{xy}^{\text{AHE}}$. The Hall resistivity can be written in terms of the Hall conductivity σ_{xy} and the longitudinal resistivity ρ_{xx} by inverting the conductivity tensor, which yields $\rho_{xy} = \sigma_{xy} \rho_{xx}^2$. In general, σ_{xy} is the sum of different contributions (ordinary and anomalous), which reflects the additivity of the Hall currents. This is especially useful when studying the anomalous Hall conductivity, σ_{xy}^{AHE} , which results from broken time-reversal symmetry in the presence of spin-orbit interaction, and may contain itself two different contributions¹. On the one hand, spin-orbit (skew) scattering produces the so-called “extrinsic” contribution, $\sigma_{xy}^{\text{AHEskew}}$, which depends linearly on the scattering rate, and thus yields a Hall resistivity directly proportional to the longitudinal resistivity, $\Delta\rho_{xy}^{\text{AHE}} \propto \rho_{xx}$. On the other hand, the so-called “intrinsic” contribution $\sigma_{xy}^{\text{AHEint}}$ is independent of the scattering rate and thus shows scaling of the form $\Delta\rho_{xy}^{\text{AHE}} \propto \rho_{xx}^2$. The intrinsic contribution is directly connected to the topology of the electronic bands². In fact, $\sigma_{xy}^{\text{AHEint}}$ can be expressed as the integral of the Berry phase curvature over occupied states in the Brillouin zone^{1,3,4}.

Broken time-reversal symmetry is a requisite for AHE, and thus the intrinsic AHE is typically observed in ferromagnets¹ and, very recently, also in non-collinear antiferromagnets with small ferromagnetic moments^{5,6}. However, here we show that a large intrinsic AHE can be induced in a non-magnetic $5d$ oxide by proximity with a ferromagnetic $3d$ oxide. This type of $3d/5d$ oxide interface has already proven an exciting playground to explore novel contributions to the intrinsic Hall effect which are related to the topological properties of correlated electrons^{7,8}. In this work we find that the AHE induced in the $5d$ oxide is very strong, has an opposite sign to that in the $3d$ ferromagnet, and it emerges due to magnetic proximity interaction. This AHE is triggered by the topological properties of the electronic states in the $5d$ oxide.

Our study focuses on interfacial magnetism and the Hall effect in $\text{La}_{0.3}\text{Sr}_{0.7}\text{MnO}_3$ (LSMO)/ SrIrO_3 (SIO or SIO-113) heterostructures. LSMO is a $3d$ half-metallic ferromagnet with strongly correlated electrons⁹. Manganites are double exchange systems where itinerant e_g electron spins are coupled by the Hund interaction to the localized t_{2g} spins. AHE in manganites is known to result from non-coplanar spin configurations of the localized t_{2g} manifolds which acquire a scalar spin chirality (real space Berry phase) acting as a virtual magnetic field in real space yielding an intrinsic (real space) contribution to the AHE^{10,11} and eventually also large topological Hall effect¹². SIO-113, a strong spin-orbit material with a paramagnetic semimetallic ground-state, has been the subject of great attention. The perovskite form of SrIrO_3 , metastable in bulk samples, is stabilized by epitaxial strain in thin films^{13–20}. Ir is in a $4+$ oxidation state, and the large octahedral crystal field stabilizes the five $5d$ electrons in a t_{2g}^5 low spin configuration^{21,22}. Angle-resolved photoemission spectroscopy has shown that the exotic semi-metallic ground state results from the heavy hole-like and light electron-like bands crossing the Fermi level¹⁹. The strong spin-orbit interaction ($0.3\text{--}0.4$ eV/atom) couples the electronic structure to a complex pattern of octahedral rotations resulting in extremely narrow bands with a bandwidth in the range of 0.3 eV where the Coulomb repulsion (with a comparable energy scale of 0.3 to 0.4 eV) results in electron correlations triggering a metal-insulator transition (MIT) in ultrathin films^{23,24}. Notably, Coulomb repulsion, spin-orbit interaction, and bandwidth with comparable energy scales conspire to establish novel electronic ground states.

Results

Sample growth and structure. Samples were epitaxially grown on (001) oriented SrTiO_3 substrates in a sputtering apparatus with a pure oxygen atmosphere at high pressures (3 mbar) and elevated temperatures (650°C for SIO and 900°C for LSMO). The structure and chemistry of the interfaces were examined by aberration-corrected scanning transmission electron microscopy (STEM) combined with electron energy loss spectroscopy (EELS) measurements. Figures 1a and 1b display high angle annular dark-field (HAADF) images of a bilayer of 4.4 nm of SIO and

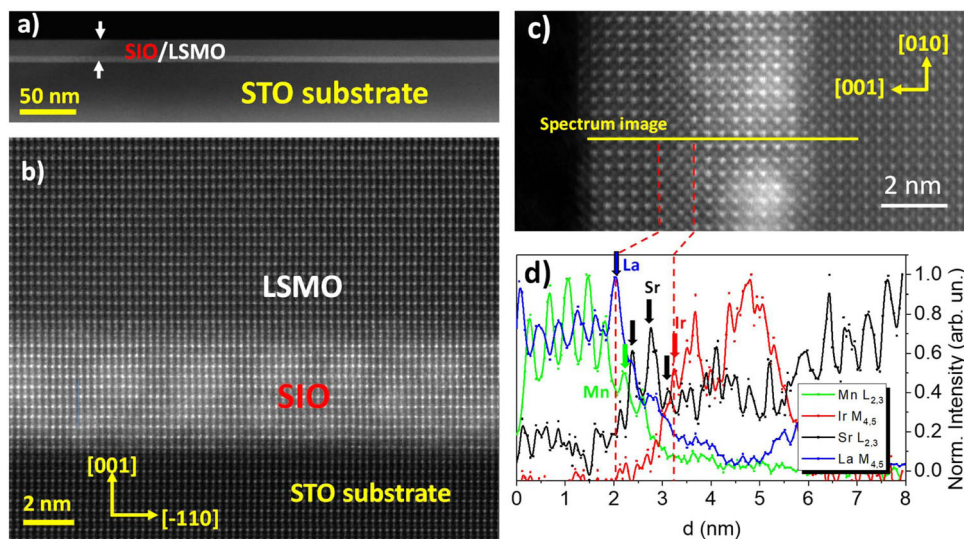


Fig. 1 Structure and chemistry of the interfaces. **a** Low magnification HAADF image of an LSMO (15 nm)/SIO (4.4 nm) sample. **b** High-resolution image of the [110] [001] SIO/LSMO interface. **c** High-resolution image of the [010] [001] LSMO (2.4 nm)/SIO (3 nm) interface and corresponding normalized intensity profile of the Mn $L_{2,3}$ (green symbols), La $M_{4,5}$ (blue symbols), and Ir $M_{4,5}$ (red symbols) and Sr $L_{2,3}$ (black symbols), of an EELS line scan acquired across the LSMO/SIO/STO interfaces.

15 nm of LSMO. The bilayers grow flat and coherent over long lateral distances, as shown in Fig. 1a. The HAADF image of Fig. 1b has been obtained from a cross-section sample thinned in the [110]/[001] plane. Since contrast scales with atomic number, the heavier Ir atoms at the B site of the perovskite (IrO₂ planes) appear brighter in the SIO, while at the LSMO side La/Sr (A site of the perovskite) is brighter. Looking at the interface a contrast anomaly can be clearly recognized, which evidences an alteration of the layer sequence at the SIO/LSMO interface. This can be further examined by combined HAADF image and EELS in a cross-section [010]/[001] sample. The spectrum image of Fig. 1c corresponds to a sample SIO (3 nm)/LSMO (2.4 nm). In this image, the heavier Ir atoms at the B site of the perovskite (IrO₂ planes) in SIO are laterally displaced with respect to the brighter La/Sr columns (A site of the perovskite) at the LSMO side. Figure 1c shows the Mn L_{2,3}, La M_{4,5}, and Sr L_{2,3} and Ir M_{4,5} integrated signals of an EELS line scan perpendicular to the interface as shown by the yellow line in Fig. 1c. Comparing the decay of the La M_{4,5} and Mn L_{2,3} signals towards the interface confirms that the SIO/LSMO interfacial plane is (La, Sr)/O. There is an extra SrO plane at the interface resulting in a LaSrO/SrO/SrO/IrO₂ layer sequence (Sr planes are marked with black arrows in Fig. 1c). The two consecutive SrO planes are displaced laterally with respect to each other as in a rock salt structure. This interface reconstruction has not been observed in other

manganite iridates superlattices^{25–27} grown by pulsed laser deposition (PLD), although it happens often at interfaces between perovskites involving members of the Ruddlesden-Popper series^{28–30}. As shown below, and similarly as in other manganite-based heterostructures³⁰, the two interfacial SrO planes will have deep implications on the interfacial magnetic properties of the heterostructures.

Transport characterization. We first studied the intrinsic Hall effect in LSMO and SIO, by measuring the Hall resistivity ρ_{xy} at low temperature ($T \leq 100$ K) in individual LSMO (thickness $d_L = 25.3$ nm) and SIO films ($d_S = 4.6 \pm 1.1$ nm). The measured ρ_{xy} includes both the contributions of the ordinary Hall effect (OHE) ρ_{xy}^{OHE} and the anomalous Hall one ρ_{xy}^{AHE} , that is, $\rho_{xy} = \rho_{xy}^{OHE} + \rho_{xy}^{AHE}$, where $\rho_{xy}^{OHE} \propto H_z$ and $\rho_{xy}^{AHE} \propto M_z$ with H_z the magnetic field and M_z the magnetization perpendicular to the film plane. Note that ρ_{xy}^{AHE} becomes constant once M_z is saturated by the applied field H_z . This allows determining ρ_{xy}^{OHE} and ρ_{xy}^{AHE} from the measured ρ_{xy} , as shown in the example of Fig. 2a for plain LSMO films. The lower panel of Fig. 2a demonstrates that ρ_{xy}^{AHE} (red line) is zero in SIO, which is expected because its ground-state is neither ferromagnetic nor ferrimagnetic, i.e., $M \sim 0$ (red line in Fig. 2b). As expected^{10,11}, there exists a finite ρ_{xy}^{AHE}

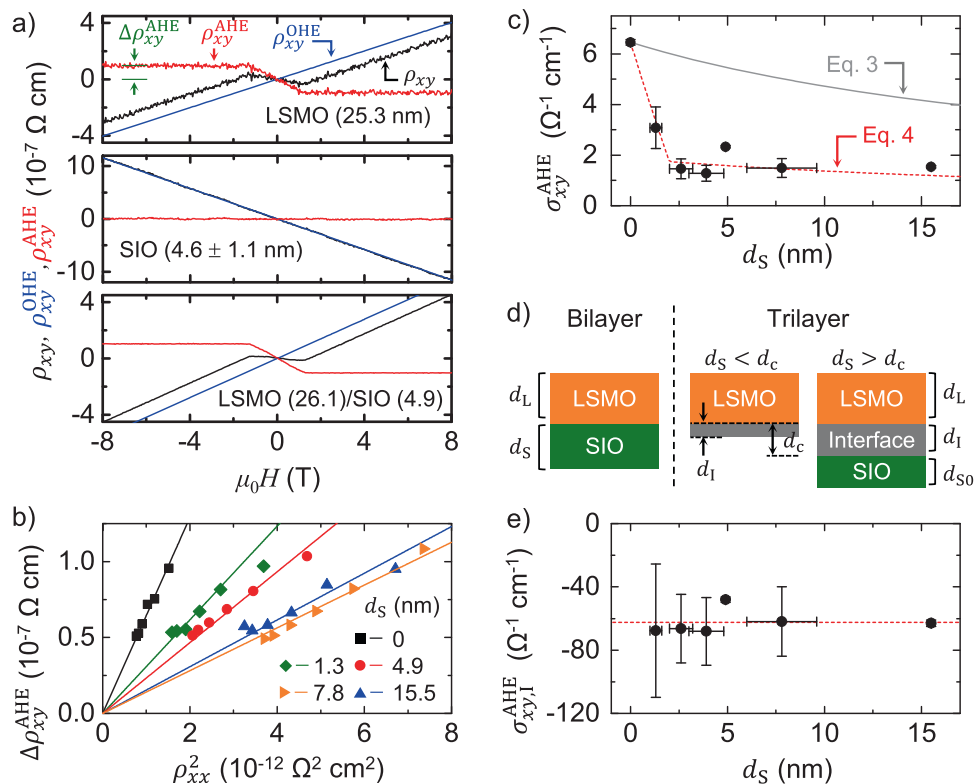


Fig. 2 Hall effect measurement and analysis. a Transverse Hall resistivity ρ_{xy} vs. out of the plane magnetic field, H_z , (black lines) of La_{0.7}Sr_{0.3}MnO₃ 25.3 nm (upper panel) and SrIrO₃ 4.6 ± 1.1 nm (middle panel) thin films and an LSMO (26.1 nm)/SIO(4.9 nm) bilayer (lower panel) measured at $T = 100$ K. Ordinary Hall resistivity ρ_{xy}^{OHE} (blue lines) and anomalous Hall resistivity, ρ_{xy}^{AHE} (red lines) have been separated. $\Delta \rho_{xy}^{AHE}$ indicates the value of ρ_{xy}^{AHE} at magnetic saturation (green arrow) **b** $\Delta \rho_{xy}^{AHE}$ vs. ρ_{xx}^2 of La_{0.7}Sr_{0.3}MnO₃/SrIrO₃ bilayers for different thicknesses d_S of SrIrO₃ (symbols). $\Delta \rho_{xy}^{AHE}$ and ρ_{xx} are measured at $T = 20, 35, 50, 65, 80,$ and 100 K for each d_S . Lines are linear fits to Eq. 1 **c** AHE conductivity, σ_{xy}^{AHE} , vs. thickness of the SrIrO₃ layer, d_S of bilayer samples. The symbols are experimental values of the Hall conductivity obtained from linear fitting curves in Fig. 2b. The gray solid line indicates the calculated σ_{xy}^{AHE} using a bilayer model (Eq. 3). To calculate σ_{xy}^{AHE} , we use $d_L = 27.3$ nm which is the average value of d_L of the different samples. The red dashed line is the calculated σ_{xy}^{AHE} using a trilayer model (Eq. 4). For the calculation, $d_c = 2$ nm and $\sigma_{xy,l}^{AHE} = -62.5 \Omega^{-1} \text{ cm}^{-1}$ are chosen. **d** Sketch illustrating the bilayer and the trilayer models used to fit Hall data (see text). **e** Calculated AHE conductivity of the interface layer, $\sigma_{xy,l}^{AHE}$, as a function of d_S using Eq. 5. For the calculation, we used $d_c = 2$ nm based on the XMCD measurements. The red dashed line indicate $\sigma_{xy,l}^{AHE} \simeq -62.5 \Omega^{-1} \text{ cm}^{-1}$ which is a mean value when $d_S > 2$ nm.

in LSMO (red line top panel of Fig. 2a), but also in the case of the LSMO/SIO bilayers (see example in the lower panel of Fig. 2a and more data in Supplementary Fig. 1). Hereinafter, we define $\Delta\rho_{xy}^{\text{AHE}}$ as the value of ρ_{xy}^{AHE} once M_z is saturated by H_z (green arrows in Fig. 2a). Note finally that the sign of the OHE in LSMO is opposite to that in SIO because carriers in manganites are holes while transport in SIO is dominated by the more mobile electrons³¹. Within a temperature range in which the magnetization is virtually constant (which is essentially the case here since $M(T)/M(0) \sim 1$ for $T \leq 100$ K), the measured $\Delta\rho_{xy}^{\text{AHE}}$ changes with the temperature only through its relationship with the longitudinal resistivity ρ_{xx} , which as discussed above, is given by the inversion of the conductivity tensor and reads:¹

$$\Delta\rho_{xy}^{\text{AHE}}(T) = \left| \sigma_{xy}^{\text{AHE}} \right| \rho_{xx}^2(T), \quad (1)$$

where σ_{xy}^{AHE} is the anomalous Hall conductivity.

In Fig. 2b, we plot $\Delta\rho_{xy}^{\text{AHE}}(T)$ as a function of $\rho_{xx}^2(T)$ for a series of bilayers having similar LSMO thickness ($d_L = 27.3 \pm 6.3$ nm) and varying SIO thickness (d_S). The set of data points for each sample (symbol type) is obtained from measurements as those in Fig. 2a taken at various temperatures ($20 \text{ K} \leq T \leq 100 \text{ K}$). A linear scaling is observed for the whole range of d_S , including the sample without SIO ($d_S = 0$). This demonstrates that the anomalous Hall conductivity is independent of the scattering rate, and thus that it is an intrinsic contribution of the AHE driven by the topological properties of Bloch states in reciprocal space (see Supplementary Figs. 2 and 3 and Supplementary Note 1 for further supporting analysis). Note in Fig. 2b that the slope of $\Delta\rho_{xy}^{\text{AHE}}$ vs. ρ_{xx}^2 , which following Eq. 1 corresponds to AHE conductivity σ_{xy}^{AHE} of the bilayer system, decreases as the SIO thickness d_S is increased. This is shown in more detail in Fig. 2c, which displays σ_{xy}^{AHE} as a function of d_S for the full series of samples (circles). An abrupt decrease of σ_{xy}^{AHE} is observed when d_S increases, followed by saturation.

In order to understand the abrupt decrease of the AHE when a few layers of SIO are put in contact with LSMO, we analyze the AHE data using a circuit model that allows calculating the transverse ρ_{xy}^{AHE} and longitudinal ρ_{xx} resistivity of a multilayer based on the individual layers'. This model and the related algebra are described in Supplementary Fig. 4 and Supplementary Note 2. If we consider a relationship between the AHE and longitudinal resistivity of the form of Eq. 1, the model yields the following expression for the AHE conductivity:

$$\sigma_{xy}^{\text{AHE}} = \frac{\Delta\rho_{xy}^{\text{AHE}}}{\rho_{xx}^2} = \frac{\sum_{i=1}^n d_i \sigma_{xy,i}^{\text{AHE}}}{\sum_{i=1}^n d_i}, \quad (2)$$

where $\Delta\rho_{xy}^{\text{AHE}}$ and ρ_{xx} are the anomalous Hall and longitudinal resistivity expected in measurement on a heterostructure composed of n different materials, each of them having a thickness d_i , and anomalous Hall conductivity $\sigma_{xy,i}^{\text{AHE}} = \Delta\rho_{xy,i}^{\text{AHE}} / \rho_{xx,i}^2$. For the case investigated here, $n = 2$ (bilayers are made of LSMO and SIO as sketched in the left panel of Fig. 2d). If we assume that both materials (LSMO and SIO) keep their intrinsic AHE resistivity when combined in the heterostructures—that is, only LSMO shows a finite $\sigma_{xy,L}^{\text{AHE}}$ while for SIO layer $\sigma_{xy,S}^{\text{AHE}} = 0$ as shown in Fig. 2a—then Eq. 2 yields:

$$\sigma_{xy}^{\text{AHE}} = \frac{d_L}{(d_L + d_S)} \sigma_{xy,L}^{\text{AHE}}, \quad (3)$$

where the AHE conductivity for LSMO $\sigma_{xy,L}^{\text{AHE}} = \Delta\rho_{xy,L}^{\text{AHE}} / \rho_{xx,L}^2$ is known through the analysis shown in Fig. 2b. Thus we can readily

calculate $\sigma_{xy}^{\text{AHE}}(d_S)$ expected from Eq. 3, which is depicted in Fig. 2c (gray line). One can see that Eq. 3 gives a slow, gradual decay of σ_{xy}^{AHE} with increasing d_S , which does not agree with the abrupt drop for small d_S —followed by near saturation—we observe in the experiments (solid circles in Fig. 2c). This shows that the assumption that LSMO and SIO keep their intrinsic AHE conductivity when combined in a heterostructure is not valid. In the following, we show that the abrupt drop in the AHE conductivity is explained by the emergence of AHE in SIO, whose sign is opposite to that in LSMO. We demonstrate below that the AHE originates in the proximity-induced magnetism in the narrow bands of the SIO.

Magnetic characterization. The magnetism in LSMO and SIO was studied by a combination of X-ray absorption spectroscopy (XAS) and X-ray magnetic circular dichroism (XMCD) at the Mn $L_{2,3}$ and Ir $L_{2,3}$ edges, conducted on samples SrTiO₃(100)//SrIrO₃ (d_S)/La_{0.7}Sr_{0.3}MnO₃ (5 nm), with $d_S = 1.2$ nm, 4 nm, and 7 nm. The low thickness of the top LSMO layer was chosen to achieve good interface sensitivity. Magnetic fields were applied in-plane in either the [100] or [110] directions. Figures 3a and 3b show absorption spectra of a bilayer sample with $d_S = 4$ nm for Ir (Fig. 3a) measured at $T = 20$ K, $\mu_0 H = 55.6$ mT and for Mn (Fig. 3b) at 50 K, $\mu_0 H = 0$ T. Measurements were conducted after field cooling in 280 mT in the case of Mn and, due to magnet limitations, in 55.6 mT in the case of Ir. The field of 55.6 mT was high enough to saturate magnetization in either field orientation (see below). XMCD measured in total electron yield (TEY) mode showed a robust magnetic moment of the Mn. XMCD spectra of the L-edge in partial fluorescence yield (PFY) mode showed clear evidence of Ir magnetic moment. Sum rules³² using L_2 and L_3 edge data at 20 K were used to obtain spin ($\langle S_z \rangle = 0.003 \pm 0.0007 \mu_B$) and orbital ($\langle L_z \rangle = 0.018 \pm 0.001 \mu_B$) moments, which were aligned antiparallel to the Mn moment. Values of spin and orbital moments estimated from PFY using sum rules are considered a rough estimate due to sources of error such as the effect of the magnetic dipole moment, T_z , on the spin moment³² and self-absorption effects (expected to be limited due to the small thickness of the samples). Square-shaped hysteresis loops of the Ir moment (see inset to Fig. 3a) measured at $T = 20$ K and $E = 11.217$ keV had a coercivity of 40 mT and 24 mT, for H applied along [100] and [110] directions, respectively. A large ratio of the orbital to spin moment $\frac{L_z}{S_z} = 6$ was found, much larger than the nominal $\frac{L_z}{S_z} = 4$ characteristic of the SIO-214²⁵, as previously reported for manganite iridate superlattices.

Induced magnetism in the iridate has been found previously in manganite/iridate superlattices with different interface reconstructions^{25–27} although, as discussed below, important differences result from our peculiar interface reconstruction. X-ray absorption spectroscopy experiments at the Ir L_3 edge for samples with different SIO thicknesses are shown in Fig. 3c. XMCD spectra did not show any measurable shift (see inset to Fig. 3c) as thickness was changed indicating that the charge transfer mechanism observed in SrMnO₃/SIO interfaces³³ is inhibited here, probably by the two interfacial SrO rock salt blocks. The main panel of Fig. 3c shows XMCD spectra around the Ir L_3 edge normalized to the XAS edge jump intensity for various samples. The XMCD peak intensity was maximum for the sample with $d_S = 1.2$ nm and reduces with increasing d_S . For $d_S = 4$ nm there is only a weak decrease of the XMCD signal while a strong suppression occurs for $d_S = 7$ nm indicating that, since XMCD is normalized to the XAS signal, only part of the SIO layer has a magnetic moment. We can estimate the thickness of the interfacial SIO layer d_I that has a magnetic moment by scaling

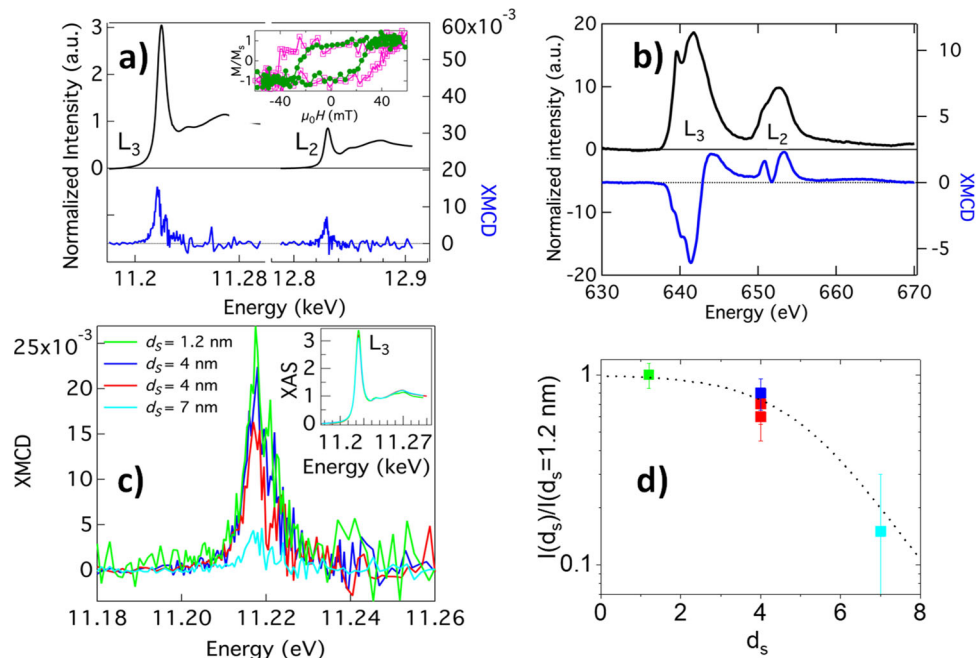


Fig. 3 X-ray absorption spectroscopy. **a** Ir $L_{2,3}$ XAS (black lines) and XMCD (blue lines) PFY spectra measured at $T = 20$ K under a saturating magnetic field of 55.6 mT applied in the [100] direction of a sample $\text{SrTiO}_3(100)/\text{SrIrO}_3(4 \text{ nm})/\text{La}_{0.7}\text{Sr}_{0.3}\text{MnO}_3(5 \text{ nm})$. Inset: L_3 Ir hysteresis loop measured at $T = 20$ K and $E = 11.217$ keV with in-plane magnetic fields along with the [100] (magenta open squares) and [110] (green circles) directions, measured from the fluorescence and X-ray reflectivity intensities, respectively. **b** Mn XAS absorption spectra (black line) and XMCD (blue line) measured in the TEY mode at $T = 50$ K at remanence after saturating in a 280 mT magnetic field applied in the [110] direction. **c** XMCD intensities for samples $\text{STO}/\text{SIO}(d_s)/\text{LSMO}(5 \text{ nm})$ at the Ir L_3 edge. For $d_s = 1.2$ nm and 7 nm, $T = 10$ K and $\mu_0 H = 60$ mT. For $d_s = 4$ nm, two nominally identical samples were measured, at various temperatures (20 K and 2 K) and magnetic fields (55.6 mT, 0.5 T). The intensity was independent of the magnetic field applied. The peak intensity at 2 K is higher than those at 20 K. Inset: Normalized XAS intensity. **d** The ratio between measured XMCD peak intensities of samples with larger SIO thicknesses and the peak intensity of the sample with the thinnest SIO $d_s = 1.2$ nm as a function of SIO thickness.

the XMCD peak intensity to that measured for $d_s = 1.2$ nm, as shown in Fig. 3d. The sigmoidal-like dotted line is a guide to the eye to show the exponential decrease of the intensity from which we estimate that $d_1 = 2$ nm. The Ir magnetic state can be discussed in connection to the atomic reconstruction of the interface uncovered by the STEM EELS experiment.

To address the origin of the induced ferromagnetism in the SIO layer separated from the LSMO by a double SrO layer, we have started by performing density functional theory (DFT) calculations on bulk SIO. We find that canted AFM ordering driven by the Dzyaloshinskii-Moriya interaction^{22,34–36} is stable when the local U on Ir d states is larger than ~ 1 eV (see Supplementary Fig. 5 and Supplementary Note 3). That is, the SIO is the neighborhood of a canted antiferromagnetic state triggered by enhanced electron correlation. Because of the small energy difference between different canted AFM states, less than ~ 10 meV/Ir, the weak superexchange interaction^{37–42} across the double SrO layers, evidenced by the antiferromagnetic alignment of the Mn and Ir moments, is enough to drive the observed magnetic state. It is worth pointing out that this superexchange interaction across double SrO layers has been observed in $\text{La}_{1.85}\text{Sr}_{0.15}\text{CuO}_4$ (LSCO-214) cuprate/manganite interfaces³⁰ where it also yields an antiferromagnetic (Cu–Mn) state.

Discussion. The finding of induced magnetism in SIO at the interface with LSMO over a nanometric length scale suggests that the unexpected drop of the AHE conductivity (Fig. 2c) with increasing SIO thickness is produced by the emergence of AHE in SIO. Based on this idea, we analyzed the AHE data by modeling the heterostructures with a trilayer model including an interface layer as sketched in Fig. 2d. In essence, we consider that the SIO

layer is divided into two sublayers: an interface layer “I” of thickness d_1 in which there exists induced magnetism and AHE, and a second layer “S0” of thickness d_{S0} in which the intrinsic properties of SIO (in particular the absence of AHE) are preserved. We assume thus that there is a characteristic length scale d_c over which the magnetic and AHE properties of SIO are affected by proximity with the LSMO. Consequently, in heterostructures in which the SIO thickness $d_s \leq d_c$, the entire SIO layer shows modified properties: $d_1 = d_s$. For heterostructures with $d_s > d_c$, $d_1 = d_c$ and $d_{S0} = d_s - d_c$. To simplify the calculations, we assume that the magnetic and electronic properties are uniform within each of the three layers d_L , d_1 and d_{S0} .

We can now apply Eq. 2 to the three-layer system, using $n = 3$, with $\sigma_{xy,S0}^{\text{AHE}} = 0$ since the intrinsic SIO properties are preserved within d_{S0} . Thus, Eq. 2 yields:

$$\sigma_{xy}^{\text{AHE}} = \frac{d_L \sigma_{xy,L}^{\text{AHE}} + d_1 \sigma_{xy,I}^{\text{AHE}}}{d_L + d_s}, \quad (4)$$

Note that $d_1, d_s, \sigma_{xy}^{\text{AHE}}$, and $\sigma_{xy,L}^{\text{AHE}}$ and d_c (the upper limit of the interfacial layer thickness d_1) can be estimated from the thickness of the layer with an induced magnetic moment at the SIO interface $d_c = 2$ nm. We can thus calculate the contribution to the anomalous Hall conductivity of the interfacial SIO layer with induced magnetism

$$\sigma_{xy,I}^{\text{AHE}} = \frac{(d_L + d_s) \sigma_{xy}^{\text{AHE}} - d_L \sigma_{xy,L}^{\text{AHE}}}{d_1}, \quad (5)$$

and plot it as a function of the SIO thickness d_s in Fig. 2e. One sees that our analysis in terms of the three-layers-model identifies an intrinsic contribution to the AHE conductivity, $\sigma_{xy,I}^{\text{AHE}}$ which is

negative and nearly independent of d_S . In the following, we discuss the topological origin of this contribution and its connection to induced magnetism in the SIO layer.

It is important to remark that these results differ from the AHE measured recently in SrMnO₃ (antiferromagnetic insulator) and SIO superlattices²⁶. In that work the appearance of magnetic moment in Ir was accompanied by changes in the magnetism of the SMO layer (which becomes ferromagnetic); and (ii) the emergence of AHE in the heterostructures was ascribed to AHE in the SMO layer, not in the SIO one. Moreover, the AHE was positive, instead of the negative AHE in our work, and was found to be in the dirty metal limit instead of the intrinsic limit of our system. It is also worth pointing out that we did not observe the topological Hall effect THE theoretically predicted⁴³ and experimentally observed⁴⁴ in similar SIO/LSMO interfaces. THE results from topological spin textures (e.g., skyrmions), and shows a characteristic signature in the Hall resistivity as (antisymmetric) “humps” superposed to the AHE and OHA signal. However, we did not observe such a signature in our samples. This can be clearly recognized in the Hall data for an SIO/LSMO shown in Fig. 2a, as well as in the raw data displayed in Supplementary Fig. 1. The THE generally appears at the interface between ferromagnets with perpendicular magnetic anisotropy and spin-orbit materials and is driven by the interfacial Dzyaloshinskii-Moriya interaction (DMI). The absence of THE in our samples is likely connected to the interface reconstruction with double SrO planes, which weakens the interfacial DMI because longer Mn-Ir distance suppresses the effect of SOC. This argument is consistent with the fact that inserting an ultrathin insulating layer between SIO and LSMO also suppresses the THE as reported earlier^{44,45}. The lack of THE, thus, rules out that the observed AHE results from non-collinear spins in the LSMO at the interface. Finally, notice that the strong negative contribution to the anomalous conductivity cannot result from a suppressed magnetization of the LSMO at the interface, which if any, would occur over a nanometric (1–2 nm) length scale producing only small changes in the anomalous Hall conductivity of the 25 nm thick LSMO layer. See Supplementary Figs. 6 and 7 and Supplementary Note 4.

The induced magnetism at the SIO interface provides an artificial realization of the necessary conditions for the AHE. Its independence on temperature (scattering rate) reflects its intrinsic character related to the topological properties of Bloch states, namely, the Berry curvature of the occupied states³. The Hall angle given by the ratio $\frac{\sigma_{xy}^{\text{AHE}}}{\sigma_{xx}}$ is typically small (well below 1%) in materials with trivial topology bands, since σ_{xy}^{AHE} is small and σ_{xx} is typically large. For the LSMO we find $\sigma_{xy}^{\text{AHE}} = 6.54(\Omega\text{cm})^{-1}$ yielding values of the anomalous Hall angle in the 0.1–0.2% (the range resulting from the temperature dependence of the longitudinal conductivity). LSMO can be regarded to have topologically trivial bands, although carriers have been proposed to acquire a real space Berry phase due to non-collinear spin structures mostly near T_C ^{10,11} and small values of the anomalous Hall conductivity are expected. On the other hand for SIO $\sigma_{xy,I}^{\text{AHE}} = -63(\Omega\text{cm})^{-1}$ is much larger, which considering $\sigma_{xx} \sim 500 - 1000(\Omega\text{cm})^{-1}$ (see Supplementary Fig. 8 and Supplementary Note 5.) yields larger values of $\frac{\sigma_{xy,I}^{\text{AHE}}}{\sigma_{xx}} \sim 6 - 13\%$. These values are comparable, yet larger, than for SrRuO₃⁷ or to MnSi^{46,47} or non-collinear antiferromagnet Mn₃Sn⁵ or CoNb₃S₆⁶ with topologically non-trivial bands. Notably, this is despite the small values of the magnetic moment induced by the interfacial proximity interaction (σ_{xy}^{AHE} which is proportional to magnetization).

The large absolute value of $\sigma_{xy,I}^{\text{AHE}}$ together with its independence on the scattering rate strongly suggests its intrinsic origin, i.e., the topological nature of the Bloch states in SIO. In fact, the topological band property in SIO has been the subject of great attention. Band structure calculations^{48,49} have shown band crossings forming a Dirac nodal ring in the U-R-X plane of the Brillouin zone. It was first proposed that its protection by the mirror symmetry of the *Pbnm* space group would render a topological semimetal. Later on, it was found that the Dirac degeneracy is lifted by epitaxial strain in thin films and that a small gap opens in thin films under epitaxial strain^{22,50}. This showed that SrIrO₃ has a Dirac line (ring) node that is protected by the *Pbnm* n-glide symmetry and is thus a non-symmorphic Dirac semimetal^{51,52}. In contrast to such Dirac semimetallic behaviors which are more closely related to non-magnetic topological systems, our LSMO/SIO systems have proximity-induced magnetism. Thus, broken time-reversal, as well as inversion symmetries, should lift the Dirac degeneracy at nodal lines or points. However, such symmetry breakings could induce robust hot spots in the Berry curvature by lifting the Dirac degeneracy⁵³. Furthermore, the stronger SOC in Ir than in Ru could lead to a much larger intrinsic AHE despite its weaker magnetism.

Theoretical analysis. In order to gain insights into the topological origin of the intrinsic AHE, we carried out theoretical analyses based on density functional theory calculations. To minimize the complexity arising from the interface with LSMO, we considered bulk SIO with the appropriate lattice constants as detailed in the “Methods” section. The proximity coupling with LSMO is simulated by performing constrained magnetic moment calculations. Here, the direction of Ir spin polarization S_{Ir} is fixed along the z direction and their magnitude is varied. We then compute the AH conductivity σ_{xy} of SIO due to “proximity-induced” magnetism. The resultant σ_{xy} is summarized in Fig. 4a as a function of the Fermi level E_F with several values of Ir spin polarization S_{Ir} and in Fig. 4b as a function of S_{Ir} with several values of E_F . Since by definition spin polarization is oppositely directed to magnetic moment, the positive SIO spin polarization corresponds to the experimental situation of Ir moments anti-aligned to Mn moments at the interface. The negative sign of σ_{xy} obtained in the calculations is thus consistent with the experiment. To our surprise, σ_{xy} reaches a very large value $-1000(\Omega\text{cm})^{-1}$ at certain condition. The non-monotonic behavior of σ_{xy} as a function of E_F or S_{Ir} , including the sign change, resembles that of SrRuO₃ as reported by Fang et al.⁷, suggesting the same origin, i.e., magnetic monopoles in momentum space. To check this scenario, we examined the Berry curvature with different parameter sets; examples are shown in Fig. 4c–f. One potential origin of the large σ_{xy} is a Dirac nodal line in the U-R-X plane in the momentum space as predicted by Zeb et al. and Carter et al.^{47,48}. This could also induce magnetic monopoles and contribute to σ_{xy} when the Fermi level E_F is close to 0, corresponding to stoichiometric SIO. At $E_F = 0$ with $S_{\text{Ir}} = 0.05$, this induces only a moderate enhancement in the Berry curvature at $(k_x, k_y, k_z) \sim (\frac{\pi}{a}, 0, \frac{\pi}{c})$ and $(\frac{\pi}{a}, 2\frac{\pi}{b}, \frac{\pi}{c})$ [see Fig. 4c] because the line node is away from $E_F = 0$. A slight enhancement in S_{Ir} is found to shift the line node closer to $E_F = 0$ and induce very sharp peaks in the Berry curvature at $(k_x, k_y, k_z) \sim (\frac{\pi}{a}, 0.25\frac{\pi}{b}, \frac{\pi}{c})$ and $(\frac{\pi}{a}, 1.75\frac{\pi}{b}, \frac{\pi}{c})$, see Fig. 4d. With some values of S_{Ir} with $E_F = 0$, the theoretical σ_{xy} could become comparable to the experimental estimation for SIO, $\sim -40\Omega^{-1}\text{cm}^{-1}$ (see Figs. 4a and 4b). At negative E_F , corresponding to hole doping, a further

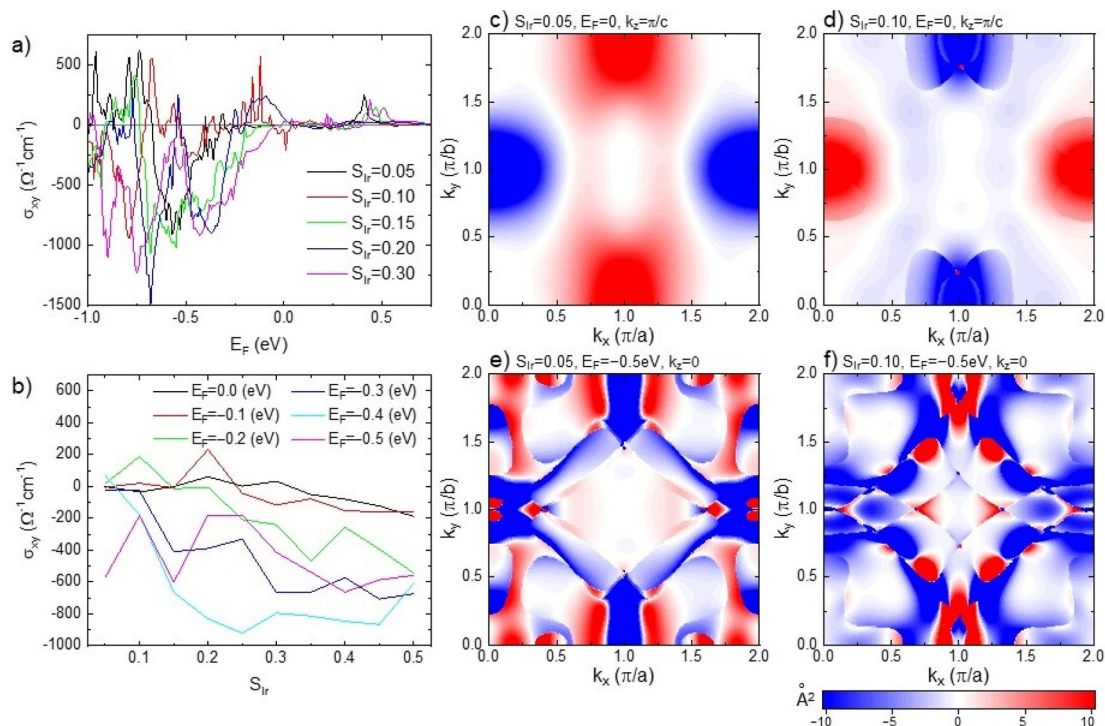


Fig. 4 Theoretical analysis. **a** Intrinsic AH conductivity **(a)** as a function of the Fermi level E_F with several values of spin polarization $S_{lr} = (n_{up} - n_{down})/2$ and **(b)** as a function of S_{lr} with several values of E_F . 2D plot of the Berry curvature for **(c)** $S_{lr} = 0.05$ at $E_F = 0$ and $k_z = \pi/c$, **(d)** $S_{lr} = 0.10$ at $E_F = 0$ and $k_z = \pi/c$, **(e)** $S_{lr} = 0.05$ at $E_F = -0.5$ eV and $k_z = 0$, and **(f)** $S_{lr} = 0.10$ at $E_F = -0.5$ eV and $k_z = 0$. $n_{up(down)}$ is the spin-up (down) electron density per Ir site.

enhancement appears, $\sigma_{xy} \sim -1000 \Omega^{-1} \text{cm}^{-1}$, as shown in Figs. 4a and 4b. This is ascribed to magnetic monopoles induced at avoided band crossings in the presence of the SOC and magnetic ordering. As shown in Figs. 4e and 4f the Berry curvature consists of multiple peaks with different magnitude and strongly supports this scenario.

To gain insight into which momentum and energy regime contributes to the large σ_{xy} , a Dirac nodal line near the U point and the stoichiometric Fermi level or avoided band crossing in hole-doped regime or both, we have analyzed band dispersion near the Fermi level and Berry curvature. Supplementary Fig. 9 shows plots of the dispersion relations near the Fermi level, 2D Fermi surfaces, and the separation between two adjacent bands, as well as Berry curvature for different cases. Nodal lines existing in non-magnetic SrIrO₃ are unstable with respect to the magnetism, i.e., nonzero magnetic moment eliminates the nodal line and opens a gap. As the magnetic moment increases, different bands move up or down, creating many different kinds of band crossings. The plots show that such band crossing indeed produces the enhancement in the Berry curvature (See Supplementary Note 6). The semi-quantitative agreement in σ_{xy} between our experimental estimation and theoretical calculations strongly suggests that the AHE in SIO-LSMO heterostructures is of topological origin, arising from magnetic monopoles in momentum space. Further analysis of the precise valence of Ir ions and induced magnetic moment may ultimately clarify the subtle difference in the location of magnetic monopoles.

A final remark is in order concerning the relative importance of the “side jump” (extrinsic) mechanism which is also independent of the scattering rate and can thus not be inferred from the relationship between the transverse and longitudinal resistivity deduced from transport measurements. As shown previously, the side-jump contribution is smaller than the

intrinsic contribution in a factor of E_{SO}/E_F which makes the intrinsic contribution dominant over a wide range of the scattering strength in clean or moderately dirty cases⁴.

In summary, the emerging intrinsic AHE observed in bilayers La_{0.7}Sr_{0.3}MnO₃/SrIrO₃ uncovers an exciting scenario of the interplay between topology and correlations at the 3d/5d interface. The symmetry breaking by the proximity-induced magnetism at the interface conspires with the strong spin-orbit interaction of the iridate to yield the hot spots of the integrated Berry curvature at nodal lines and band anticrossings, providing an artificial realization of the minimal model of the AHE³. It is very important that, despite the small values of the magnetic moment induced in the iridate by proximity to the manganite, the amplification by the topological properties of the iridate is so large that the anomalous Hall angle reaches values among the largest reported in the literature. The theoretical results show that the topological amplification of the AHE we have uncovered can be made even larger by hole doping, opening the door to the external tuning topological properties, an intriguing new direction towards future topological spintronics and spin-orbitronics at correlated oxide interfaces⁵⁴ with strong spin-orbit interaction.

Methods

Sample growth. Samples were grown using a high-pressure sputtering system in a pure oxygen (2.8 mbar) atmosphere from stoichiometric La_{0.7}Sr_{0.3}MnO₃ (LSMO) and SrIrO₃ (SIO) targets. The growth temperature was 650 °C for SIO and 900 °C for LSMO. The high-pressure growth allows for a high degree of thermalization of extracted species before they arrive in the substrate. This technique has shown epitaxial growth of oxides with good epitaxial properties^{37,39}.

STEM EELS. Aberration-corrected scanning transmission electron microscopy (STEM) and electron energy loss spectroscopy (EELS) measurements have been obtained using a JEOL JEM ARM200cF operated at 200 kV using a condenser lens aperture of 1 mm. The specimens were prepared by mechanical grinding and polishing and Ar ion milling at grazing incidence in a Fischione 1010 ion mill. To

get information about detailed plane sequence cross-section samples were prepared in [100] and [110] zone axes. EELS composition line scans were measured at element-specific absorption edges (Mn $L_{2,3}$, La $M_{4,5}$, and Ir $M_{4,5}$, Sr $L_{2,3}$) using a Gatan Quantum EEL spectrometer in dual EELS mode. EELS intensities at element-specific lines were obtained from multiple linear least-square (MLLS) methods.

Transport measurements. The longitudinal and transverse dc resistances, R_{xx} and R_{xy} , were measured as a function of the magnetic field H (applied perpendicular to the film plane) for different temperatures in the range 5–300 K using a closed-cycle refrigerator equipped with a superconducting magnet. The resistance is defined as $R_{xx} = V_{xx}/I_{xx}$ and $R_{xy} = V_{xy}/I_{xx}$, with I_{xx} the injected dc current and V_{xx} and V_{xy} the voltages measured parallel and perpendicular to the injected current. Voltage offsets were removed by inverting the current sign and averaging the measured voltage. The pure Hall signal, which is “odd” with respect to the applied field, was calculated as $(R_{xy}(H) + R_{xy}(-H) - R_{xy}(H) - R_{xy}(-H))/2$. This allows removing any spurious contribution to R_{xy} resulting from the electrodes’ misalignment and the strong magnetoresistance of LSMO (which is “even” with respect to the applied field). We calculated the resistivity ρ_{xx} and ρ_{xy} via the Van der Pauw method from the resistances obtained as described above, by considering the films’ dimensions and thickness.

X-ray measurements. X-ray absorption spectroscopy (XAS) and X-ray magnetic circular dichroism (XMCD) measurement were conducted at the Advanced Photon Source (Argonne National Laboratory). The Mn $L_{2,3}$ edge was probed at the APS beamline 4-ID-C (soft X-rays) and the total electron yield (TEY) and reflectivity signals were measured. The Ir $L_{2,3}$ edge was probed at the APS beamline 4-ID-D (hard X-rays), where the partial fluorescence yield and reflectivity signals were measured.

DFT calculations. First-principles DFT calculations were performed using the generalized gradient approximation⁵⁵ and the projector augmented wave (PAW) pseudopotentials⁵⁶ as implemented in the Vienna ab initio Simulation Package (VASP) code^{57,58}. To better describe the strong correlation effect, the local Hubbard repulsion⁵⁹ with $U = 2$ eV is included for Ir d states⁶⁰. The spin-orbit coupling (SOC) is also turned on. To minimize the complexity arising from the interface with LSMO, we considered bulk SIO with the experimental lattice constants, $a = 5.5617$ Å, $a = 5.5909$ Å, and $c = 7.8821$ Å with corrections^{61,62}. The proximity coupling with LSMO is simulated by performing constrained magnetic moment calculations. Here, the direction of Ir moments is fixed along the crystallographic z direction and their size is varied.

Following a self-consistent calculation with total energy convergence of 10^{-5} eV, the maximally localized Wannier functions⁶³ were constructed using the WANNIER90 code⁶⁴ from the *ab initio* ground-state wave function. In the disentanglement process, 112 Wannier functions were chosen as initial projections including the d orbitals of Ir atoms and the p orbitals of O atoms. Finally, the AHC was calculated by computing the Berry curvature using the Wannier interpolation approach which is also implemented in the WANNIER90 code^{64,65}.

Data availability

Data are available upon request from the authors.

Received: 17 June 2020; Accepted: 25 April 2021;

Published online: 02 June 2021

References

- Nagaosa, N., Sinova, J., Onoda, S., MacDonald, A. H. & Ong, N. P. Anomalous Hall effect. *Rev. Mod. Phys.* **82**, 1539–1592 (2010).
- Haldane, F. D. M. Berry curvature on the fermi surface: anomalous hall effect as a topological fermi-liquid property. *Phys. Rev. Lett.* **93**, 206602 (2004).
- Onoda, S., Sugimoto, N. & Nagaosa, N. Intrinsic versus extrinsic anomalous hall effect in ferromagnets. *Phys. Rev. Lett.* **97**, 126602 (2006).
- Onoda, S., Sugimoto, N. & Nagaosa, N. Quantum transport theory of anomalous electric, thermoelectric, and thermal Hall effects in ferromagnets. *Phys. Rev. B* **77**, 165103 (2008).
- Nakatsuji, S., Kiyohara, N. & Higo, T. Large anomalous Hall effect in a non-collinear antiferromagnet at room temperature. *Nature* **527**, 212–215 (2015).
- Ghimire, N. J. et al. Large anomalous Hall effect in the chiral-lattice antiferromagnet CoNb3S6. *Nat. Commun.* **9**, 1–6 (2018).
- Fang, Z. et al. The anomalous Hall effect and magnetic monopoles in momentum space. *Science* **302**, 92–95 (2003).
- Matsuno, J. et al. Interface-driven topological Hall effect in SrRuO₃-SrIrO₃ bilayer. *Sci. Adv.* **2**, e1600304 (2016).
- Imada, M., Fujimori, A. & Tokura, Y. Metal-insulator transitions. *Rev. Mod. Phys.* **70**, 1039–1263 (1998).
- Lyanda-Geller, Y. et al. Charge transport in manganites: hopping conduction, the anomalous Hall effect, and universal scaling. *Phys. Rev. B* **63**, 184426 (2001).
- Ye, J. et al. Berry phase theory of the anomalous hall effect: application to colossal magnetoresistance manganites. *Phys. Rev. Lett.* **83**, 3737–3740 (1999).
- Vistolli, L. et al. Giant topological Hall effect in correlated oxide thin films. *Nat. Phys.* **15**, 67–72 (2019).
- Nichols, J. et al. Tuning electronic structure via epitaxial strain in Sr₂IrO₄ thin films. *Appl. Phys. Lett.* **102**, 141908 (2013).
- Nichols, J. et al. Anisotropic electronic properties of a-axis-oriented Sr₂IrO₄ epitaxial thin-films. *Appl. Phys. Lett.* **103**, 131910 (2013).
- Wu, F.-X. et al. Metal-insulator transition in SrIrO₃ with strong spin-orbit interaction. *J. Phys. Condens. Matter* **25**, 125604 (2013).
- Biswas, A., Kim, K. S. & Jeong, Y. H. Metal insulator transitions in perovskite SrIrO₃ thin films. *J. Appl. Phys.* **116**, 213704 (2014).
- Gruenewald, J. H. et al. Compressive strain-induced metal-insulator transition in orthorhombic SrIrO₃ thin films. *J. Mater. Res.* **29**, 2491–2496 (2014).
- Zhang, L. et al. Tunable semimetallic state in compressive-strained SrIrO₃ films revealed by transport behavior. *Phys. Rev. B* **91**, 35110 (2015).
- Nie, Y. F. et al. Interplay of spin-orbit interactions, dimensionality, and octahedral rotations in semimetallic SrIrO₃. *Phys. Rev. Lett.* **114**, 16401 (2015).
- Liu, J. et al. Tuning the electronic properties of $J_{\text{eff}}=1/2$ correlated semimetal in epitaxial perovskite SrIrO₃. *arXiv* 1305.1732 (2013).
- Moon, S. J. et al. Dimensionality-controlled insulator-metal transition and correlated metallic state in 5d transition metal oxides Sr_{n+1}Ir_nO_{3n+1} ($n=1, 2$, and ∞). *Phys. Rev. Lett.* **101**, 226402 (2008).
- Kim, B. J. et al. Phase-sensitive observation of a spin-orbital Mott state in Sr₂IrO₄. *Science* **323**, 1329–1332 (2009).
- Groenendijk, D. J. et al. Spin-Orbit semimetal SrIrO₃ in the two-dimensional limit. *Phys. Rev. Lett.* **119**, 256403 (2017).
- Schütz, P. et al. Dimensionality-driven metal-insulator transition in spin-orbit-coupled SrIrO₃. *Phys. Rev. Lett.* **119**, 256404 (2017).
- Yia, D. et al. Atomic-scale control of magnetic anisotropy via novel spin-orbit coupling effect in La_{2/3}Sr_{1/3}MnO₃/SrIrO₃ superlattices. *Proc. Natl Acad. Sci. USA* **113**, 6397–6402 (2016).
- Nichols, J. et al. Emerging magnetism and anomalous Hall effect in iridate-manganite heterostructures. *Nat. Commun.* **7**, 1–6 (2016).
- Yi, D. et al. Tuning perpendicular magnetic anisotropy by oxygen octahedral rotations in (La_{1-x}Sr_xMnO₃)/ (SrIrO₃) superlattices. *Phys. Rev. Lett.* **119**, 77201 (2017).
- Matvejef, M., Chikyow, T. & Lippmaa, M. Interface growth of La_{1.2}Sr_{1.8}Mn_{1.7}Ru_{0.3}O₇ Ruddlesden-Popper films on SrTiO₃. *J. Cryst. Growth* **311**, 1201–1205 (2009).
- Nie, Y. F. et al. Atomically precise interfaces from non-stoichiometric deposition. *Nat. Commun.* **5**, 1–8 (2014).
- De Luca, G. M. et al. Ubiquitous long-range antiferromagnetic coupling across the interface between superconducting and ferromagnetic oxides. *Nat. Commun.* **5**, 5626 (2014).
- Manca, N. et al. Balanced electron-hole transport in spin-orbit semimetal SrIrO₃ heterostructures. *Phys. Rev. B* **97**, 81105 (2018).
- Laguna-Marco, M. A. et al. Orbital magnetism and spin-orbit effects in the electronic structure of BaIrO₃. *Phys. Rev. Lett.* **105**, 216407 (2010).
- Okamoto, S. et al. Charge transfer in iridate-manganite superlattices. *Nano Lett.* **17**, 2126–2130 (2017).
- Matsuno, J. et al. Engineering a spin-orbital magnetic insulator by tailoring superlattices. *Phys. Rev. Lett.* **114**, 247209 (2015).
- Hao, L. et al. Two-dimensional $J_{\text{eff}} = 1/2$ antiferromagnetic insulator unraveled from interlayer exchange coupling in artificial perovskite iridate superlattices. *Phys. Rev. Lett.* **119**, 27204 (2017).
- Hao, L. et al. Giant magnetic response of a two-dimensional antiferromagnet. *Nat. Phys.* **14**, 806–810 (2018).
- Garcia-Barriocanal, J. et al. Spin and orbital Ti magnetism at LaMnO₃/SrTiO₃ interfaces. *Nat. Commun.* **1**, 1–7 (2010).
- Cuellar, F. A. et al. Reversible electric-field control of magnetization at oxide interfaces. *Nat. Commun.* **5**, 1–8 (2014).
- Bruno, F. Y. et al. Insight into spin transport in oxide heterostructures from interface-resolved magnetic mapping. *Nat. Commun.* **6**, 1–9 (2015).
- Okamoto, S. Magnetic interaction at an interface between manganite and other transition metal oxides. *Phys. Rev. B* **82**, 24427 (2010).
- Salafranca, J. & Okamoto, S. Unconventional proximity effect and inverse spin-switch behavior in a model manganite-cuprate-manganite trilayer system. *Phys. Rev. Lett.* **105**, 256804 (2010).
- Luca, G. M. De et al. Ubiquitous long-range antiferromagnetic coupling across the interface between superconducting and ferromagnetic oxides. *Nat. Commun.* **5**, 1–7 (2014).
- Mohanta, N., Dagotto, E. & Okamoto, S. Topological Hall effect and emergent skyrmion crystal at manganite-iridate oxide interfaces. *Phys. Rev. B* **100**, 064429 (2019).

44. Li, Y. et al. Emergent topological Hall effect in $\text{La}_{0.7}\text{Sr}_{0.3}\text{MnO}_3/\text{SrIrO}_3$ Heterostructures. *ACS Appl. Mater. Interfaces* **11**, 21268–21274 (2019).
45. Skoropata, E. et al. Interfacial tuning of chiral magnetic interactions for large topological Hall effects in $\text{LaMnO}_3/\text{SrIrO}_3$ heterostructures. *Sci. Adv.* **6**, eaaz3902 (2020).
46. Lee, M., Onose, Y., Tokura, Y. & Ong, N. P. Hidden constant in the anomalous Hall effect of high-purity magnet MnSi. *Phys. Rev. B* **75**, 172403 (2007).
47. Neubauer, A. et al. Topological hall effect in the α phase of MnSi. *Phys. Rev. Lett.* **102**, 186602 (2009).
48. Zeb, M. A. & Kee, H. Y. Interplay between spin-orbit coupling and Hubbard interaction in SrIrO_3 and related Pbnm perovskite oxides. *Phys. Rev. B* **86**, 85149 (2012).
49. Carter, J. M., Shankar, V. V., Zeb, M. A. & Kee, H. Y. Semimetal and topological insulator in perovskite iridates. *Phys. Rev. B* **85**, 115105 (2012).
50. Liu, Z. T. et al. Direct observation of the Dirac nodes lifting in semimetallic perovskite SrIrO_3 thin films. *Sci. Rep.* **6**, 1–9 (2016).
51. Fang, C., Chen, Y., Kee, H. Y. & Fu, L. Topological nodal line semimetals with and without spin-orbital coupling. *Phys. Rev. B* **92**, 81201 (2015).
52. Liu, J. et al. Strain-induced nonsymmorphic symmetry breaking and removal of Dirac semimetallic nodal line in an orthoperovskite iridate. *Phys. Rev. B* **93**, 85118 (2016).
53. Liu, E. et al. Giant anomalous Hall effect in a ferromagnetic kagome-lattice semimetal. *Nat. Phys.* **14**, 1125–1131 (2018).
54. Tokura, Y., Kawasaki, M. & Nagaosa, N. Emergent functions of quantum materials. *Nat. Phys.* **13**, 1056–1068 (2017).
55. Perdew, J. P., Burke, K. & Ernzerhof, M. Generalized gradient approximation made simple. *Phys. Rev. Lett.* **77**, 3865–3868 (1996).
56. Blöchl, P. E. Projector augmented-wave method. *Phys. Rev. B* **50**, 17953–17979 (1994).
57. Kresse, G. & Furthmüller, J. Efficient iterative schemes for ab initio total-energy calculations using a plane-wave basis set. *Phys. Rev. B* **54**, 11169–11186 (1996).
58. Kresse, G. & Joubert, D. From ultrasoft pseudopotentials to the projector augmented-wave method. *Phys. Rev. B* **59**, 1758–1775 (1999).
59. Dudarev, S. & Botton, G. Electron-energy-loss spectra and the structural stability of nickel oxide: An LSDA+U study. *Phys. Rev. B* **57**, 1505–1509 (1998).
60. Arita, R., Kune, J., Kozhevnikov, A. V., Eguiluz, A. G. & Imada, M. Ab initio studies on the interplay between spin-orbit interaction and coulomb correlation in Sr_2IrO_4 and Ba_2IrO_4 . *Phys. Rev. Lett.* **108**, 86403 (2012).
61. Zhao, J. G. et al. High-pressure synthesis of orthorhombic SrIrO_3 perovskite and its positive magnetoresistance. *J. Appl. Phys.* **103**, 103706 (2008).
62. Puggioni, D. & Rondinelli, J. M. Comment on ‘high-pressure synthesis of orthorhombic SrIrO_3 perovskite and its positive magnetoresistance’ [J. Appl. Phys. 103, 103706 (2008)]. *J. Appl. Phys.* **119**, 86102 (2016).
63. Marzari, N. & Vanderbilt, D. Maximally localized generalized Wannier functions for composite energy bands. *Phys. Rev. B* **56**, 12847–12865 (1997).
64. Mostofi, A. A. et al. wannier90: a tool for obtaining maximally-localised Wannier functions. *Comput. Phys. Commun.* **178**, 685–699 (2008).
65. Wang, X., Yates, J. R., Souza, I. & Vanderbilt, D. Ab initio calculation of the anomalous Hall conductivity by Wannier interpolation. *Phys. Rev. B* **74**, 195118 (2006).

Acknowledgements

The authors acknowledge received funding from the projects Quantox of QuantERA ERA-NET Cofund in Quantum Technologies (Grant Agreement No. 731473) and To2Dox of the Flag ERA ERA-NET implemented within the European Union’s Horizon 2020 Programme. This work was supported by Spanish MINECO through grants, MAT2017-87134-C02, J.S. thanks Scholarship program Alembert funded by the IDEX

Paris-Saclay, ANR-11-IDEX-0003-02. Work at CNRS/Thales lab supported by ERC grant N° 647100 “SUSPINTRONICS” and French ANR grants ANR-15-CE24-0008-01 “SUPERTRONICS” and ANR-17-CE24-0026-03 “OISO”. J.S. thanks Maria Varela for helpful discussions. L.F.L. was supported by the China Scholarship Council. The research at ORNL was supported by the US Department of Energy (DOE), Office of Science, Basic Energy Sciences, Materials Sciences, and Engineering Division. Computational studies were carried out at the Advanced Computing Facility (ACF) of the University of Tennessee Knoxville, as well as Compute and Data Environment for Science (CADES) at the Oak Ridge National Laboratory, which is supported by the Office of Science of the U.S. Department of Energy under Contract No. DE-AC05-00OR22725. Work at Bryn Mawr was supported by NSF (DMR #1708790). Work by S.G.E.T.V. and S.R. (x-ray experiments and analysis) was supported by the U.S. Department of Energy, Office of Science, Basic Energy Sciences, Materials Sciences, and Engineering Division. This research used resources of the Advanced Photon Source, a U.S. Department of Energy (DOE) Office of Science User Facility operated for the DOE Office of Science by Argonne National Laboratory under Contract No. DE-AC02-06CH11357.

Author contributions

M.W.Y. and A.S. measured the Hall effect and M.W.Y. analyzed and modeled data. J.T., A.P., D.S.-M., F.G., A.R., C.L. grew samples and characterized structure, M.C., G.S.-S., and J.M.G.-C. did the microscopy, L.-F.L., N.M., E.D., S.O. did the theory, D.H., J.W.F., D.J.K., Y.Ch., J.S., X.W., S.R., St.V., H.B.V., M.V. did the magnetic characterization (x-ray absorption and neutron reflectometry), St.V., S.O., M.W.Y., J.S., and J.E.V. wrote the manuscript, J.S. and J.E.V. designed the experiment. The results were discussed and interpreted by all the authors cited so far, with contributions from M.B., A.B., A.A. All authors discussed results and revised the manuscript.

Competing interests

The authors declare no competing interests.

Additional information

Supplementary information The online version contains supplementary material available at <https://doi.org/10.1038/s41467-021-23489-y>.

Correspondence and requests for materials should be addressed to J.S.

Peer review information *Nature Communications* thanks Kathrin Dörr, Jiadong Zang and the other, anonymous, reviewer(s) for their contribution to the peer review of this work.

Reprints and permission information is available at <http://www.nature.com/reprints>

Publisher’s note Springer Nature remains neutral with regard to jurisdictional claims in published maps and institutional affiliations.



Open Access This article is licensed under a Creative Commons Attribution 4.0 International License, which permits use, sharing, adaptation, distribution and reproduction in any medium or format, as long as you give appropriate credit to the original author(s) and the source, provide a link to the Creative Commons license, and indicate if changes were made. The images or other third party material in this article are included in the article’s Creative Commons license, unless indicated otherwise in a credit line to the material. If material is not included in the article’s Creative Commons license and your intended use is not permitted by statutory regulation or exceeds the permitted use, you will need to obtain permission directly from the copyright holder. To view a copy of this license, visit <http://creativecommons.org/licenses/by/4.0/>.

© The Author(s) 2021